Mechanical Systems and Signal Processing 257 (2026) 114426

Contents lists available at ScienceDirect

Mechanical Systems and Signal Processing

journal homepage: www.elsevier.com/locate/ymssp

Full Length Article

Gaussian-process-based sensor placement and uncertainty quantification for dynamic response reconstruction in flexible aeroelastic structures

Boge Dong [a], Yihan Mei [a], Xuanyi Lu [b], Yi Zhou [a], Shenghan Zhang [b], Wenjia Wang [c], Molong Duan [a,*]

[a] Department of Mechanical and Aerospace Engineering, The Hong Kong University of Science and Technology, Hong Kong, China
[b] Department of Civil and Environmental Engineering, The Hong Kong University of Science and Technology, Hong Kong, China
[c] Department of Industrial Systems Engineering and Management, National University of Singapore, Singapore

ARTICLE INFO

Keywords:
Aeroelastic measurement
Gaussian process
Uncertainty quantification
Fiber optic sensing
Flexible aircraft
Wind tunnel tests

ABSTRACT

Accurate sensing of dynamic aeroelastic response is crucial for the safety and performance of flexible aircraft. Although a variety of data-driven neural-network approaches, in-situ inverse estimation schemes, and modal-analysis-based identification methods have been investigated for aeroelastic shape reconstruction, existing approaches still lack providing globally consistent deformation fields with quantified uncertainty prediction under realistic sensor sparsity and complex loading. This work introduces a Gaussian-process-based fiber optic sensing framework for aeroelastic measurement and flexible structural health monitoring that links fiber optic sensing placement to the spanwise uncertainty distribution. The fiber optic sensing placements are modeled as Gaussian process models with closed-form posterior mean and variance for each deformation degree of freedom, using nonstationary hyperparameters informed by Lipschitz-regularized aerodynamic loading to capture spatially varying correlations and provide credible uncertainty estimates at both instrumented and uninstrumented locations. Continuous sensor paths on shell structure surfaces are parameterized in a reduced-order form using conformal mapping and non-uniform rational B-splines. Path design is then formulated as a posterior uncertainty minimization problem to identify information-optimal paths for shape reconstruction. Simulation and wind tunnel tests on a flexible wing prototype demonstrate a significant reduction in posterior uncertainty relative to straight and sinusoidal baselines, together with substantial improvements in displacement and rotation reconstruction accuracy.

1. Introduction

Aeroelastic phenomena are pivotal in modern aircraft design, arising from the coupling between aerodynamic loads and structural deformation. The influence intensifies in flexible configurations that pursue higher efficiency through elongated, slender wings. Such configurations increase lift production while reducing induced drag at a given flight speed relative to conventional rigid wings [1].

* Corresponding author at: The Hong Kong University of Science and Technology, Room 2570, Academic Building, Clear Water Bay, Kowloon, Hong Kong, China.

E-mail addresses: bdongab@connect.ust.hk (B. Dong), ymeiak@connect.ust.hk (Y. Mei), xuanyi.lu@connect.ust.hk (X. Lu), yzhouev@connect.ust.hk (Y. Zhou), ceshenghan@ust.hk (S. Zhang), wenjiawang@nus.edu.sg (W. Wang), duan@ust.hk (M. Duan).

https://doi.org/10.1016/j.ymssp.2026.114426
Received 18 December 2025; Received in revised form 14 April 2026; Accepted 13 May 2026
Available online 10 June 2026

However, structural flexibility introduces amplified deformations, reduced flutter margins, heightened susceptibility to dynamic vibrations and limit-cycle oscillations, and elevated risk of divergence and structural failure [2]. Precise aeroelastic measurements are therefore essential for ensuring flight safety and maintaining structural integrity across the operational envelope.

Accordingly, sensing technologies capable of capturing structural response with high fidelity are critical. The common aeroelastic measurement hardware includes strain gauges [3], photogrammetry [4], and fiber optic sensing (FOS) [5,6]. Strain gauges remain prevalent owing to low cost and technological maturity, converting elastic deformation into changes in electrical resistance that are read via a Wheatstone bridge circuit (WBC) [7]. Lokos et al. [8] developed a strain-gauge calibration framework using single-point, multi-point, and distributed loading to derive load equations for shear, bending moment, and torque for an aeroelastic fighter wing. Extending strain-gauge-based load measurement from static calibration to dynamic conditions, Bighashdel et al. [9] proposed an analytical method that accounts for the modal and elastic characteristics of the measurement system, enhancing the strain-gauge performance on unsteady aerodynamic force estimation. However, signal degradation over long distances, as well as high sensitivity to noise and temperature [10], limits usage primarily to laboratory or ground-test verification rather than in-flight aeroelastic measurement applications. Apart from strain gauges, photogrammetry is a technology that obtains deformation data through the process of recording, measuring, and interpreting photographic images [11]. Graves et al. [3] utilized a single-camera photogrammetry system to capture dynamic deformation in a business-jet wing–fuselage model for modal identification. Figueiredo et al. [4] proposed a computer-vision approach to estimate aerostructural natural frequencies. However, the vision-based method has high requirements for light conditions and high-contrast markers, limiting its application in outdoor or dynamically changing environments [12]. Motivated by these limitations, recent research increasingly emphasizes FOS sensors for aeroelastic measurements [13–17] due to advantages over strain gauges and vision-based systems, including immunity to electromagnetic interference, higher resolution and bandwidth, lower mass, and simplified installation. Kressel [13] deployed a fiber Bragg grating (FBG) sensor network on an unmanned aerial vehicle (UAV) for the in-flight load monitoring tests. Lance et al. [14] developed a Fiber Optic Sensing System (FOSS) for a morphing-wing UAV to monitor two-dimensional wing deformation. However, global aeroelastic deformation is inferred from limited local strain, rendering estimation accuracy highly dependent on FOS sensor placement; robust reconstruction strategies and optimized FOS placement are required to support reliable structural health monitoring.

The choice of global deformation estimation algorithm is critical to accurately reconstructing structural response from limited in-situ measurements. The most widely used deformation reconstruction methods are the inverse Finite Element Method (iFEM) [18], Ko Displacement Theory [19], and Modal Analysis [20]. Gherlone et al. [18] introduced the iFEM with the Timoshenko beam theory to reconstruct the sectional strain of a circular tube via in-situ strain gauge measurements. William et al. [19] proposed the Ko Displacement Theory, which utilizes straight FOS sensors and cross-section geometry to reconstruct tapered wing bending and torsional displacement. Cazzulani et al. [20] proposed use of the Fisher Information Matrix and Modal Analysis to maximize information capturing of the FOS sensor placement for the model identification of the plate. Despite their successes, these methods have important limitations when applied to complex aeroelastic structures. Ko Displacement Theory assumes straight FOSs aligned with neutral axes and simplified cross-sectional behavior, which is restrictive for curved, anisotropic, or variable-stiffness structures. Modal-analysis-based reconstruction generally relies on a linear dynamic representation and a limited set of extracted modal characteristics, which may reduce reconstruction accuracy when complex coupling or nonlinearity is presented. Therefore, in this work, iFEM would be adopted for global aeroelastic deformation estimation, which is broadly applicable to complex geometries and load cases because it does not require material constitutive laws or external load knowledge.

Besides reconstruction algorithms, aeroelastic estimation accuracy also depends strongly on the FOS sensors' placement. Primary optimization targets include shape-sensing improvements [21–24], modal identification [20,25], and damage-detection [26,27]. However, these optimization objectives typically either ignore uncertainty quantification or treat uncertainty as a single scalar metric, providing limited insight into the spatial distribution of prediction confidence across the structure. To address this shortcoming, recent work has begun to introduce Gaussian process (GP) models for structural mechanics applications. The GP is a probabilistic data-driven model that generalizes multivariate Gaussian distributions to infinite-dimensional function spaces, enabling flexible, non-parametric regression [28] in high-dimensional, small-sample, and nonlinear settings [29–31]. Hendriks et al. [32] adapted the GP framework to recover two-dimensional strain fields from diffraction measurements, explicitly modeling the associated uncertainty. In a related development, Poloni et al. [33] introduced a pre-extrapolation strategy that leverages GP to estimate predicted uncertainty in extrapolative regions and uses this as a basis for determining functional weights, so that regions with larger uncertainty are down-weighted. These efforts demonstrate the potential of GP-based uncertainty quantification in structural response estimation, but they do not yet provide a cohesive framework for linking FOS surface placement to spatially resolved predicted uncertainty on realistic three-dimensional (3D) aeroelastic geometries.

This work proposes an uncertainty-quantification framework that estimates the spatial beam element strain uncertainty along the longitudinal axis of a 3D aeroelastic shell structure and explicitly links FOS surface placement to GP posterior predicted uncertainty in the reconstructed deformation. The main contributions are as follows.

- A Gaussian-process-based sensor placement framework for dynamic aeroelastic measurement is proposed that explicitly links sensor locations to the spatial posterior uncertainty distribution of sectional strain elements, thereby aligning placement decisions with reconstruction accuracy.
- A nonstationary Gaussian process kernel is constructed whose local variance magnitude and length scales are adapted using Lipschitz-regularized aerodynamic loading, so that regions with rapidly varying loads or deformation are modeled with higher resolution and better calibrated uncertainty.

- Sensor placement is optimized to minimize posterior uncertainty, with conformal mapping and Non-uniform rational B-spline parameterization representing continuous fiber-optic sensing paths on curved shell surfaces in a low-dimensional design space, substantially reducing the complexity of distributed sensor path optimization.
- The proposed method is verified in simulations and wind tunnel experiments on a flexible wing prototype, demonstrating reduced posterior uncertainty and improved displacement and rotation reconstruction accuracy relative to baseline straight and sinusoidal paths.

The paper is organized as follows: Section 2 introduces the GP theory. Section 3 details the establishment of the GP-based sensor placement optimization framework. Section 4 illustrates the flexible wing design and the reconstruction verification of the proposed methods via simulation and wind tunnel tests.

2. Background on Gaussian process

The GP is a non-parametric Bayesian approach for modeling distributions over functions. A GP is defined as a collection of random variables, any finite subset of which follows a multivariate Gaussian distribution. Formally, a GP is defined as

$$f(x) \sim \mathscr{GP}(0, k(x,x)), \tag{1}$$

where $x \in \mathbb{R}$, $f(x)$ is the function of interest, $k(x,x)$ is the covariance kernel that determines the correlation between function values at different inputs, and 0 denotes the zero mean of the Gaussian process model. The choice of the kernel function is based on the smoothness and likely patterns to be observed in the data. Usually, the common choices for kernel functions are the Radial Basis Function (RBF) kernel [28], which is given by

$$k(x,x') = \nu_f^2 \exp\left(\frac{-\|x-x'\|^2}{2l^2}\right), \quad \forall i,j \in \{1,\cdots,n\}, \tag{2}$$

where ν_f^2 is the signal variance hyperparameter, controlling the signal's average distance away from the function's mean, and l is the length scale hyperparameter, determining the reach of correlations between inputs.

Suppose that observations $\mathbf{y}_t = (y_1,\cdots,y_t)$ are collected at input points $\mathbf{x}_t = \{x_1,\cdots,x_t\}$, where the observations are assumed to be noisy realizations of the true underlying function $f(\mathbf{x}_t) = (f(x_1),\cdots,f(x_t))$, i.e.,

$$\mathbf{y}_t = f(\mathbf{x}_t) + \eta, \quad \eta \sim \mathscr{N}(0, \nu^2 I), \tag{3}$$

where η denotes noise, ν^2 is the noise variance and I represents the identity matrix. Accordingly, the noise observations satisfy

$$\mathbf{y}_t \sim \mathscr{N}(0, K(\mathbf{x}_t,\mathbf{x}_t) + \nu^2 I). \tag{4}$$

For a set of test points $\mathbf{x} = \{x'_1 \cdots x'_n\}$ and under the assumption of a zero-mean GP prior, the corresponding function $f(\mathbf{x}) = (f(x'_1) \cdots f(x'_n))$ follow

$$f(\mathbf{x}) \sim \mathscr{N}(0, K(\mathbf{x},\mathbf{x})). \tag{5}$$

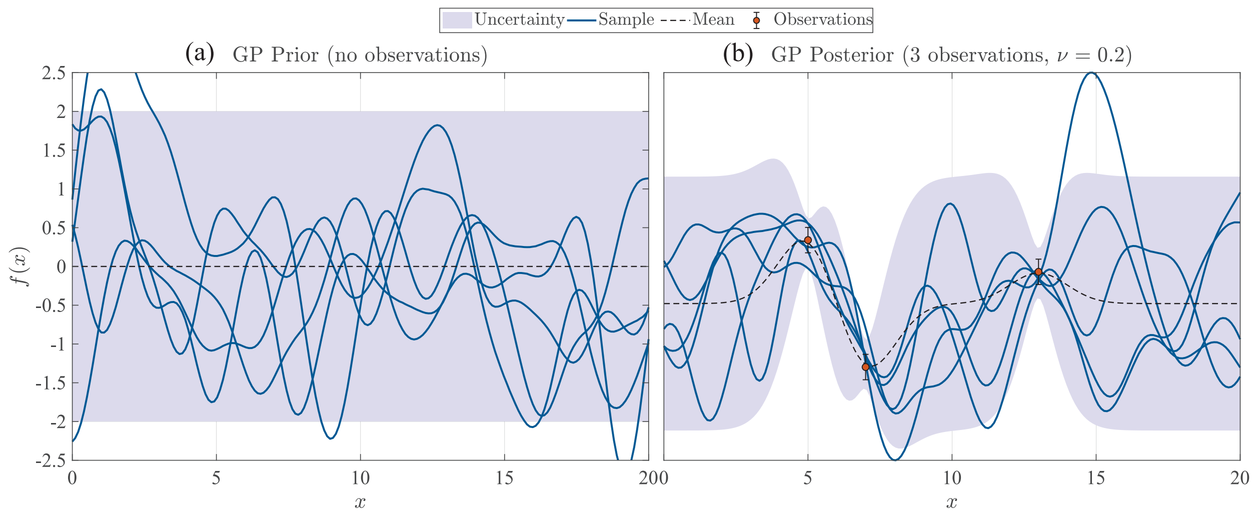

Fig. 1. Gaussian process prior and posterior illustration on a 1D example, with the consideration of measurement noise.

Therefore, by the properties of GP, i.e., $(\mathbf{y}_t, f(\mathbf{x}))$, the joint distribution of $\mathbf{y}_t$ and $f(\mathbf{x})$ follows a multivariate normal distribution and is written as

$$\begin{bmatrix} \mathbf{y}_t \\ f(\mathbf{x}) \end{bmatrix} \sim \mathscr{N}\left(\begin{bmatrix} 0 \\ 0 \end{bmatrix}, \begin{bmatrix} K(\mathbf{x}_t, \mathbf{x}_t) + v^2 I & K(\mathbf{x}_t, \mathbf{x}) \\ K(\mathbf{x}, \mathbf{x}_t) & K(\mathbf{x}, \mathbf{x}) \end{bmatrix} \right), \tag{6}$$

where $K(\mathbf{x}_t, \mathbf{x}_t)$ is the covariance matrix of the observation data, $K(\mathbf{x}, \mathbf{x})$ is the covariance matrix of the points of interest, $K(\mathbf{x}_t, \mathbf{x})$ is the covariance matrix between observations and points of interest, and $K(\mathbf{x}, \mathbf{x}_t)$ is the covariance matrix between points of interest and observed points. The predicted mean and variance based on the observation data are

$$\begin{aligned} \mu(\mathbf{x}) &= K(\mathbf{x}, \mathbf{x}_t)\left[K(\mathbf{x}_t, \mathbf{x}_t) + v^2 I\right]^{-1} \mathbf{y}_t, \\ \sum(\mathbf{x}) &= K(\mathbf{x}, \mathbf{x}) - K(\mathbf{x}, \mathbf{x}_t)\left[K(\mathbf{x}_t, \mathbf{x}_t) + v^2 I\right]^{-1} K(\mathbf{x}_t, \mathbf{x}). \end{aligned} \tag{7}$$

The samples from a GP prior with a radial basis function kernel are illustrated in Fig. 1, alongside the posterior mean and variances after incorporating three observations with noise considerations. Generally, a prior is the assumptions that may be based on historical data, theory, expert experience, or subjective judgment. The presence of noise indicates that the predicted mean value will not exactly match the measurement, and the predicted uncertainty will not be reduced to zero. It highlights the data-driven nature of GP, as more data are added, the predicted mean becomes more accurate, and the uncertainty shrinks in the vicinity of the observations.

3. Gaussian-process-based FOS sensor placement framework

3.1. Challenges in the FOS sensor placement

The FOS sensors bonded to shell structural surfaces provide distributed measurements of deformation and aeroelastic response. However, the FOS sensor has a limited number of sensing points and inherently records only axial strain along the fiber path, limiting direct access to transverse, shear, and out-of-plane components and complicating reconstruction of global deformation. In this work, we propose to model the shell structure as beam elements and decompose the measured strain into axial strain, torsional strain, shear strain, and curvatures, as illustrated in Fig. 2. These fields are then integrated to recover the sectional rotation and centerline displacement, subject to the appropriate boundary conditions. Sensor placement and data fusion are cast within a GP-based framework to regularize the reconstruction and quantify uncertainty in the inferred strain fields.

Consider geometries such as circular tubes, square beams, and airfoil wings that can be represented by a centerline $C(x)$ and an associated cross-section $C_s(x)$. The centerline is aligned with the structural longitudinal direction, and each cross-section is assumed to remain parallel to the root-frame's $y-z$ plane. The displacement of the centerline and the rotation of each cross-section with respect to the root's longitudinal axis are defined as

$$\mathbf{u}(x) = \begin{bmatrix} u(x) & v(x) & w(x) & \theta_x(x) & \theta_y(x) & \theta_z(x) \end{bmatrix}^\top, \tag{8}$$

where $u(x)$, $v(x)$, and $w(x)$ represent the displacement of the centerline. $\theta_x(x)$, $\theta_y(x)$, and $\theta_z(x)$ are the rotations with respect to the body frame. Within brackets, variable x denotes longitudinal coordinate. Furthermore, neglecting warping and invoking the small-strain assumption with Timoshenko beam theory, the surface strain and the non-zero beam-element strain components are expressed as follows [34]

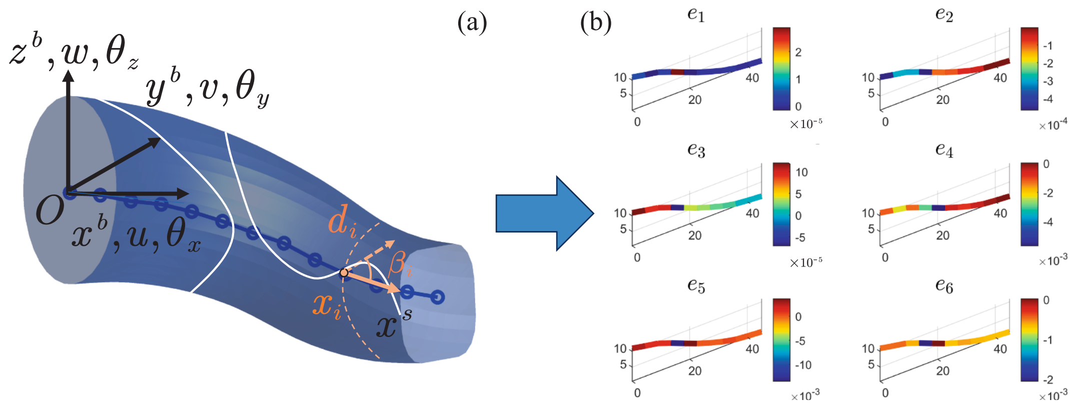

Fig. 2. Illustration of FOS sensors placed on the shell structure surfaces with their equivalent beam model, and reconstructed beam element strains. x_i, d_i, and β_i are the spanwise sensing location, contour position on the cross-section, and local fiber orientation angle with respect to the local centerline x^s.

$$\begin{aligned} \varepsilon_x^b &= e_1(x) + z_{cs}(x)e_2(x) + y_{cs}(x)e_3(x), \\ \gamma_{xy}^b &= e_5(x) - z_{cs}(x)e_6(x), \\ \gamma_{xz}^b &= e_4(x) + y_{cs}(x)e_6(x), \end{aligned} \tag{9}$$

where ε_x^b denotes the normal strain, and γ_{xy}^b and γ_{xz}^b represent shear strain under the body frame. Terms $y_{cs}(x)$ and $z_{cs}(x)$ represent the cross-section coordinates of the sensing point. The arbitrary beam strain vector $\boldsymbol{e}(\mathbf{u}) = [\, e_1 \quad e_2 \quad e_3 \quad e_4 \quad e_5 \quad e_6 \,]^\top$ denotes the beam element's axial, bending, shear, and torsional strain, which are derived as

$$\begin{aligned} e_1 &= \frac{\partial u}{\partial x}, & e_4 &= \frac{\partial w}{\partial x} + \theta_y, \\ e_2 &= \frac{\partial \theta_y}{\partial x}, & e_5 &= \frac{\partial v}{\partial x} - \theta_z, \\ e_3 &= -\frac{\partial \theta_z}{\partial x}, & e_6 &= \frac{\partial \theta_x}{\partial x}. \end{aligned} \tag{10}$$

With sectional strain mathematically defined, the inverse mapping from measured surface strains to sectional strains becomes pivotal for 3D beam-shape reconstruction. Since surface strains are available only at limited sensing locations, an inverse mapping is proposed to estimate the continuous sectional strain field consistent with this data. The beam-element strain field reconstruction accuracy strongly depends on the sensor placement and could be quantified via GP posterior uncertainty analysis. To explicitly manage uncertainty during optimization, a framework for FOS deployment that jointly optimizes variables, including (i) sensing locations x_i, (ii) cross-sectional contour distance specified by d_i with respect to the positive axis, and (iii) fiber orientations β_i relative to the local centerline, subject to manufacturing constraints, such as maximal allowable curvature, total length, and avoidance of self-intersection. Considering a sensing point of the FOS sensor, its surface measurement of a sensing point follows the standard strain-transformation relation, in which the normal strain along an arbitrary fiber direction is obtained by projecting the in-plane strain tensor onto the fiber orientation. Specifically, the sensing fiber is attached along a direction defined by the angle β_i in the local shell coordinates, and the measured strain also corresponds to the local strain field, which is characterized by $\varepsilon_{11}^s(x_i, d_i)$, $\varepsilon_{22}^s(x_i, d_i)$, and $\gamma_{12}^s(x_i, d_i)$. Its measured surface strain is defined as [18]

$$\varepsilon_m(x_i, d_i, \beta_i) = \varepsilon_{11}^s(x_i, d_i)\cos^2(\beta_i) + \varepsilon_{22}^s(x_i, d_i)\sin^2(\beta_i) + \gamma_{12}^s(x_i, d_i)\cos(\beta_i)\sin(\beta_i), \tag{11}$$

where the subscript denotes the i th strain sensor on the FOS. Terms ε_{11}^s, ε_{22}^s, and γ_{12}^s denote the in-plane normal strain in the x direction, normal strain in the y direction and the shear strain under the shell element local coordinate, respectively. Assume the relationship of $\varepsilon_{11}^s = -\nu\varepsilon_{22}^s$, where ν is the Poisson ratio. Eq. (11) is rewritten as

$$\varepsilon_m(x_i, d_i, \beta_i) = \varepsilon_{11}^s(x_i, d_i)\big(\cos^2(\beta_i) - \nu\sin^2(\beta_i)\big) + \gamma_{12}^s(x_i, d_i)\cos(\beta_i)\sin(\beta_i). \tag{12}$$

Surface strains vector are converted from the body frame to the local shell frame via the local direct cosine matrix (DCM) as

$$\boldsymbol{\varepsilon}^s(x) = T(x)\boldsymbol{\varepsilon}^b(x). \tag{13}$$

Considering small-strain kinematics and local coordinate projection, Eq. (12) is derived from Eq. (9), yielding

$$\begin{aligned} \varepsilon_{11}^b &= e_1 + e_2 z_{cs}(x_i, d_i) + e_3 y_{cs}(x_i, d_i), \\ \gamma_{12}^b &= e_4 - e_5 + e_6\big(y_{cs}(x_i, d_i) + z_{cs}(x_i, d_i)\big), \end{aligned} \tag{14}$$

where $y_{cs}(x)$ and $z_{cs}(x)$ are the cross-sectional coordinates of the sensing point in the body frame. Substituting Eq. (13) and Eq. (14) into Eq. (11), yields the relationship between the measured surface strain and the reconstructed beam strain component

$$\begin{aligned} \varepsilon_m(x_i, d_i, \beta_i) &= \left(\begin{bmatrix} g_1(\beta_i) & 0 & 0 \\ 0 & 0 & g_1(\beta_i) \\ 0 & g_1(\beta_i) & 0 \\ g_2(\beta_i) & 0 & 0 \\ -g_2(\beta_i) & 0 & 0 \\ 0 & g_2(\beta_i) & g_2(\beta_i) \end{bmatrix} \begin{bmatrix} 1 \\ y_{cs}(x_i, d_i) \\ z_{cs}(x_i, d_i) \end{bmatrix} \right)^\top \begin{bmatrix} e_1^\varepsilon(x_i) \\ e_2^\varepsilon(x_i) \\ e_3^\varepsilon(x_i) \\ e_4^\varepsilon(x_i) \\ e_5^\varepsilon(x_i) \\ e_6^\varepsilon(x_i) \end{bmatrix} \\ &= q(x_i, d_i, \beta_i)\boldsymbol{e}^\varepsilon(x_i) \end{aligned} \tag{15}$$

where

$$g_1(\beta_i) = T_{11}\left(\cos^2(\beta_i) - \nu\sin^2(\beta_i)\right) + T_{31}\cos(\beta_i)\sin(\beta_i),$$
$$g_2(\beta_i) = T_{13}\left(\cos^2(\beta_i) - \nu\sin^2(\beta_i)\right) + T_{33}\cos(\beta_i)\sin(\beta_i), \tag{16}$$

where $T_{ab}, \forall a, b \in \{1, 2, 3\}$ represents terms in the DCM matrix T. Eq. (15) successfully establishes six sectional strain terms from the FOS sensor measurement and its placement, which provides a theoretical basis for the GP posterior uncertainty analysis.

3.2. Gaussian process model considering FOS sensor placement

Full field strain is not directly observable from the FOS sensor measurements. To maximize information under limited sensing and to quantify confidence at both measured and unmeasured locations, the GP regression is adopted to model the spatial correlation of sectional strains, yielding a probabilistic reconstruction of the equivalent beam-element strain field along the longitudinal direction with spanwise posterior uncertainty. It is worth noting that the GP modeling adopted in this work is introduced as a modeling assumption to enable tractable prediction and uncertainty quantification, rather than to assert that the aeroelastic response is strictly Gaussian.

Assume the beam-strain field indexed by the axial coordinate x admits a Gaussian prior as in Eq. (1). Departing from conventional scalar GP formulations, the six sectional strain terms defined in Eq. (10) are assembled into a vector-valued latent field

$$\mathbf{e}(x) = [\, e_1(x) \quad e_2(x) \quad e_3(x) \quad e_4(x) \quad e_5(x) \quad e_6(x) \,]^\top, \tag{17}$$

which is modeled as a matrix-valued Gaussian process,

$$\mathbf{e}(x) \sim \mathscr{GP}(\overline{\mathbf{e}}(x), \mathbf{K}(x, x^{'} d_t, \beta_t)\,), \tag{18}$$

where $\overline{\mathbf{e}}(x) \in \mathbb{R}^6$ is the mean function and $\mathbf{K}(x, x' d_t, \beta_t) \in \mathbb{R}^{6\times 6}$ is the cross-covariance kernel matrix with the FOS sensor's position hyperparameters d_t and β_t. The (i,j)-th entry of $\mathbf{K}(x, x' d_t, \beta_t)$, denoted by $k_{ij}(x, x' d_t, \beta_t)$, characterizes the covariance between the i-th and j-th sectional strain components at two spanwise locations x and x' respectively. Reconstructed sectional strains are denoted as

$$\mathbf{e}^\varepsilon(x) = \mathbf{e}(x) + \boldsymbol{\eta}^\varepsilon, \quad \boldsymbol{\eta}^\varepsilon \sim \mathscr{N}\left(0, \nu_t^2 \mathbf{I}\right), \tag{19}$$

where $\boldsymbol{\eta}^\varepsilon$ denotes an additional error term accounting for measurement, modeling, and manufacturing imperfections, with a total variance ν_t^2. Term $\mathbf{I}$ is the identity matrix.

Kernel selection critically governs the representation of spatial correlation in strain measurements. In aeronautical structures, strain along a wing exhibits nonstationary behavior due to non-uniform loads, such as engine thrust, aerodynamic lift, and torque. A nonstationary kernel is therefore adopted, allowing covariance to adapt locally in both amplitude and smoothness. For the sectional strain field, define

$$\mathbf{k}(x, x') = \mathbf{v}(x)\exp\left(\frac{-(x - x')^2}{2}\mathbf{l}^{-1}(x)\mathbf{l}^{-1}(x')\right)\mathbf{v}(x'), \tag{20}$$

where $\mathbf{v}(x) \in \mathbb{R}^{6\times 6}$, and $\mathbf{l}(x) \in \mathbb{R}^{6\times 6}$ denotes spatially varying uncertainty and length-scale matrices, respectively. To relate functional smoothness to the covariance kernel, the derivative process is characterized by the mixed partials of the kernel

$$\mathbf{e}^{'}(x) = \frac{\partial^2 \mathbf{k}(x, x')}{\partial x \partial x'}. \tag{21}$$

Under a locally stationary approximation, the variance of the derivative satisfies

$$\mathrm{Var}(\mathbf{e}^{'}(x)\,) = \left.\frac{\partial^2 \mathbf{k}(x, x')}{\partial x \partial x'}\right|_{x=x'} \approx \mathbf{v}(x)\mathbf{l}^{-1}(x)\mathbf{l}^{-1}(x')\mathbf{v}(x'). \tag{22}$$

Impose a global upper bound on the pointwise rate of change via the Lipschitz constant

$$\widetilde{\boldsymbol{L}}_{\max}(x) := \sup|\mathbf{e}(x)|. \tag{23}$$

Assume the Lipschitz constant is proportional to the standard deviation of the derivative process

$$\widetilde{\boldsymbol{L}}_{\max}(x) \propto \sqrt{\mathrm{Var}(\mathbf{e}'(x)\,)} = \mathbf{v}(x)\mathbf{l}^{-1}(x). \tag{24}$$

Once $\widetilde{\boldsymbol{L}}_{\max}(x)$ and $\mathbf{v}(x)$ are determined from sensor hardware specifications and simulation or experimental data, respectively, the global smoothness constraint and the corresponding closed-form expression for the nonstationary length scale are obtained as

$$\mathbf{l}(x) = \mathbf{v}(x)\widetilde{\boldsymbol{L}}_{\max}^{-1}(x). \tag{25}$$

To connect the nonstationary kernel with the hyperparameters d_t and β_t, the idea of propagation of covariance [35] is applied

$$\mathbf{K}(\mathbf{x}_t, \mathbf{x}_t, d_t, \beta_t) = \mathbf{Q}(\mathbf{x}_t, d_t, \beta_t)\mathbf{k}(\mathbf{x}_t, \mathbf{x}_t)\mathbf{Q}(\mathbf{x}_t, d_t, \beta_t)^{\top} + v_t^2\mathbf{I}_m, \tag{26}$$

where matrix $\mathbf{Q}(\mathbf{x}_t, d_t, \beta_t)$ denotes the concatenation of the $q(x_i, d_i, \beta_i)$ matrix defined in Eq. (15). Consequently, the predicted beam-element strain and corresponding posterior uncertainty with respect to the longitudinal axis are constructed below

$$\begin{aligned} \boldsymbol{e}^{\varepsilon}(\mathbf{x}) &= \mathbf{k}(\mathbf{x}, \mathbf{x}_t)\mathbf{Q}^{\top}[\mathbf{K}(\mathbf{x}_t, \mathbf{x}_t, d_t, \beta_t)]^{-1}\mathbf{Q}(\mathbf{Q}^{-1}\varepsilon_m), \\ \mathbf{v}^{\varepsilon}(\mathbf{x}) &= \mathbf{k}(\mathbf{x}, \mathbf{x}) - \mathbf{k}(\mathbf{x}, \mathbf{x}_t)\mathbf{Q}^{\top}[\mathbf{K}(\mathbf{x}_t, \mathbf{x}_t, d_t, \beta_t)]^{-1}\mathbf{Q}\mathbf{k}(\mathbf{x}_t, \mathbf{x}), \end{aligned} \tag{27}$$

where $\mathbf{v}^{\varepsilon} = [v_1^{\varepsilon}(x) \quad v_2^{\varepsilon}(x) \quad v_3^{\varepsilon}(x) \quad v_4^{\varepsilon}(x) \quad v_5^{\varepsilon}(x) \quad v_6^{\varepsilon}(x)]^{\top}$. The GP is parameterized along the longitudinal coordinate and incorporates FOS sensor placement-dependent hyperparameters, yielding closed-form posterior means and pointwise uncertainties for the sectional strain field. This probabilistic formulation quantifies confidence at measured and unmeasured locations and explicitly accounts for measurement, modeling, and manufacturing noise, providing a rigorous basis for assessing reconstruction accuracy.

3.3. Reduced-order FOS sensor path via conformal mapping and non-uniform rational B-spline parameterization

The representation of the FOS sensor path in 3D space is challenging for optimization due to an infinite degree of freedom (DOF). In this work, the optimization employs conformal mapping [36] with non-uniform rational B-spline (NURBS) parameterization to reduce the DOF of the FOS sensor path and the associated computational complexity. Most 3D shell structures are non-developable; consequently, any mapping to a plane inevitably induces stretching or compression. Quasi-conformal maps preserve angles but not metric lengths, thereby producing local length-distortion factors. Consider a 3D shell geometry $\mathscr{S}(x, y, z)$ mapped conformally to an unfolded planar domain $\mathscr{M}(\widehat{u}, \widehat{v})$ via $\widehat{f}: \mathscr{S} \rightarrow \mathscr{M}$, which is then discretized into a triangular mesh with nodal connectivity. To ensure the uniformly distributed sensing points in the FOS sensor in the 3D geometry and project into the 2D domain, the distortion brought from conformal mapping should be considered, which can be derived as [37]

$$r_d = \frac{\partial \mathscr{S}}{\partial \mathscr{M}}. \tag{28}$$

The conformal mapping and the corresponding distortion map are illustrated in Fig. 3. For a developable cylinder, r_d is constant, whereas for non-developable geometries, such as spheres and airfoils, r_d varies spatially.

Moreover, NURBS parameterization is exploited to represent the 3D FOS sensor path as

$$\mathbf{c}_3(\xi) = \sum_{\zeta=1}^{n_c} N_{\zeta,m}(\xi)\mathbf{p}_{3,\zeta}, \tag{29}$$

where $\xi \in [0, 1]$ is the B-spline curve parameter, n_c is the number of control points, $\mathbf{p}_{3,\zeta}$ is the ζ th control point, and $N_{\zeta,m}(\xi)$ is the ζ th normalized m-order B-spline basis function defined as

$$N_{\zeta,1}(\xi) = \begin{cases} 1, & \xi_{\zeta} \leq \xi < \xi_{\zeta+1} \\ 0, & \text{otherwise} \end{cases}, \tag{30}$$

$$N_{\zeta,m}(\xi) = \frac{(\xi - \xi_{\zeta})N_{\zeta,m-1}(\xi)}{\xi_{\zeta+m-1} - \xi_{\zeta}} + \frac{(\xi_{\zeta+m} - \xi)N_{\zeta+1,m-1}(\xi)}{\xi_{\zeta+m} - \xi_{\zeta+1}}. \tag{31}$$

Note that ξ_i is the knot in a non-decreasing sequence of real numbers $[\xi_1, \cdots, \xi_{n_c+m}]$ called the knot vector. Assume the FOS sensor is represented by a m-order B-spline with n_c control points $\mathbf{p}_{3,1}, \mathbf{p}_{3,2}, \ldots, \mathbf{p}_{3,n_c}$, where each control point $\mathbf{p}_{3,\zeta} \in \mathbb{R}^3$. These control points are concatenated into a control point matrix $\mathbf{P}_3 \in \mathbb{R}^{n_c \times 3}$ given by

$$\mathbf{P}_3 = [\mathbf{p}_{3,1}, \mathbf{p}_{3,2}, \ldots, \mathbf{p}_{3,n_c}]^{\top}. \tag{32}$$

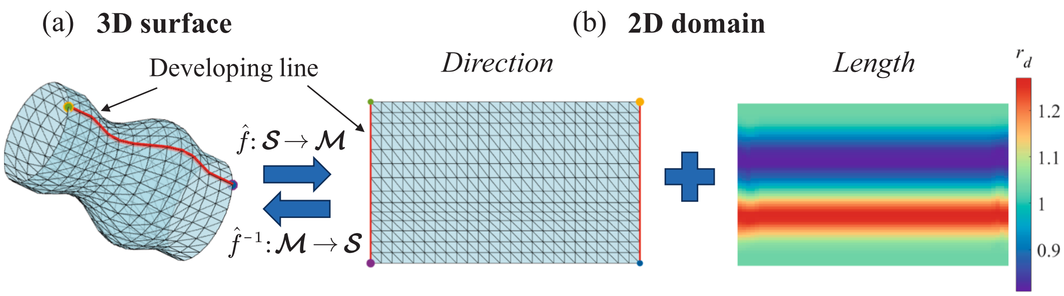

Fig. 3. The bijective conformal mapping and its distortion map.

The 3D FOS path is expressed as the weighted combination of the 3D control points through the corresponding basis functions, which is given by

$$\mathbf{c}_3(\xi, \mathbf{P}_3) = \mathbf{N}^{(i)}(\xi)\mathbf{P}_3, \tag{33}$$

where $\mathbf{N}^{(i)}(\xi)$ is the vector combination of the set of basis functions of the i th B-spline. To further reduce the optimization complexity, convert 3D control points into a 2D domain, denoted as

$$\mathbf{P}_2 = r_d^{-1}\widehat{f}(\mathbf{P}_3), \tag{34}$$

where each 2D control point is equivalent to the coordinates of the sensing point, which are obtained as (x_i, d_i), and the orientation β_i is then determined from the local tangent direction of the continuous path. Moreover, the accurate projection of uniformly distributed 3D sensing points onto the 2D parameter domain is essential for reliable uncertainty evaluation. Thus, the arc-length parameterization of the $\mathbf{c}_3$ is given by

$$\mathbf{L}_3(\xi) = \int_0^{\xi} \left\| \frac{d\mathbf{c}_3}{d\xi} \right\| d\xi, \tag{35}$$

where $|\cdot|$ denotes the Euclidean norm. A sequence of n equidistant points along the 3D FOS sensor path are defined by the arc-length values

$$s_3 = \frac{\mathbf{L}_3(1)}{n-1}, \;\; n > 1, \tag{36}$$

where $\mathbf{L}_3(1)$ is the total length of the FOS path, and the arc length parameter is conveniently obtained as

$$\xi_h = \mathbf{L}_3^{-1}(h \cdot s_3), \forall h \in [0, \cdots, n-1]. \tag{37}$$

Assume that all the B-spline parameterizations have the same order and knot spacing. Therefore, the basis functions are identical for the same number of control points and knot vector, i.e., $\mathbf{N}^{(i)}(\xi) = \mathbf{N}^{(j)}(\xi)$ if $n_c^{(i)} = n_c^{(j)}$. Thus, the path in the 2D plane with the corresponding sensing points distribution is given by $\mathbf{c}_2(\xi_h, \mathbf{P}_2)$. It simplifies the path expression in the optimization process, while ensuring the nature of uniformly distributed sensing points in the 3D FOS sensor to build valid uncertainty evaluations.

3.4. Optimization setup

The optimization of FOS sensor placement aims to reduce the posterior uncertainty of the reconstructed beam strains by manipulating the 2D control points on the unfolded 3D geometry, while satisfying manufacturing constraints. The overall optimization is defined as

$$\begin{aligned} &\min_{\mathbf{P}_2} J = a_1 C_{GP} + a_2 L, \\ &\text{s.t. } \kappa_k < \overline{\kappa}, k = 1, \cdots, L, \\ &\qquad \mathbf{c}_2(\xi_1, \mathbf{P}_2) \neq \mathbf{c}_2(\xi_2, \mathbf{P}_2), \;\; \forall \xi_1 \neq \xi_2, \;\; \xi_1, \xi_2 \in [0, 1], \end{aligned} \tag{38}$$

where C_{GP} aggregates the normalized posterior uncertainty of the six beam strain components, which is given by

$$C_{GP} = \frac{\mathbf{v}^{\varepsilon}}{\|\mathbf{v}^{\varepsilon}\|}. \tag{39}$$

Term L is the total length of the FOS path. Physically, it has a dual interpretation: besides representing material usage, it also reflects the number of effective sensing points and the spatial coverage of the distributed FOS. Accordingly, L acts as a trade-off term between reconstruction quality and practical manufacturability. The coefficients a_1 and a_2 are preference parameters that balance uncertainty reduction and path length. The curvature condition is introduced to enforce manufacturability by limiting the extent to which a candidate FOS path violates the allowable bending constraint during optimization. In the numerical implementation, this condition is treated as a soft constraint and is defined as

$$C_{\kappa} = \sum_{k=1}^{L} e^{(|\kappa_k| - \overline{\kappa})}, \tag{40}$$

where the local curvature κ_k is computed from three adjacent control points, and deviations beyond the maximal allowance curvature $\overline{\kappa}$ are penalized. In addition, the self-intersection condition is introduced to prevent path crossing on the unfolded surface and thereby ensure geometric feasibility of the FOS layout.

The overall GP-based FOS placement optimization framework is shown in Fig. 4. Even with a probabilistic objective, FOS placement design in structural health monitoring often exhibits nonconvexity, discontinuities, and combinatorial variables. As a result, stochastic optimizers, such as the genetic algorithm (GA), are employed. The process iteratively evaluates the objective function with the manipulation of the 2D NURBS control points. Once converged, the optimized control points $\mathbf{P}_2^*$ and the optimized part posterior uncertainty information is outputted. The Gaussian-process-based optimization framework connects uncertainty quantification from GP posterior analysis to the GA optimizer through the objective function. Specifically, the GP model is used for response prediction and posterior uncertainty estimation, which serves as the main cost metric in the cost function for evaluating candidate fiber-optic sensor paths.

4. Flexible wing simulation and experiment verification

4.1. Flexible wing design and experiment platform

Practical implementations of flexible wings typically assume trimmed flight. To excite substantial deformation across all six degrees of freedom, such as axial extension, torsion, bidirectional bending, and biaxial shear, the takeoff phase is considered, with all control surfaces deflected to their maximum limits. Such a configuration generally yields the highest aerodynamic loading on the wing structure, thereby producing the most informative deformation response for evaluation and sensing design. In the wind tunnel experiment, the control surfaces are driven with step and sinusoidal inputs to demonstrate that the optimized path effectively captures dynamic aeroelasticity.

To simulationally and experimentally validate the proposed GP-based optimized FOS sensor placement strategy, a specialized flexible wing prototype was designed and manufactured. The prototype is illustrated in Fig. 5, which comprises five modular airfoil sections, each featuring a 205 mm span and 230 mm chord length, interconnected by a 1100 mm central carbon fiber tube. Each airfoil section incorporated an actively controlled surface capable of $\pm$ 20° deflection, actuated by KST X10 mini digital servos. Force measurements were obtained using an ATI Mini85 load cell mounted at the wing root, with complete system specifications detailed in Tables 1–3. The load cell measures forces and moments at the wing root. The difference between lift and shear force is negligible in the case of the low-frequency vibration and steady-flow wind tunnel experiment [38]. In static cases, the measured shear force equals the lift, which is the sum of aerodynamic forces perpendicular to the airfoil surface. In dynamic cases, the measurement also includes inertia forces from vibration. In this study, the vibration frequency and magnitude are small; thus, inertia forces are generally negligible compared to the lift [39].

Digital servos are controlled via a Beckhoff TwinCAT real-time control system operating at 200 Hz sampling frequency, utilizing both EtherCAT and RS-485 communication protocols. Digital servo actuators were precisely calibrated using a KEYENCE LK-503 1D profiler to establish the nonlinear relationship between control surface deflection angles and servo duty cycles.

The distributed strain measurement system incorporated a LUNA ODiSI 6100 optical distributed sensors interrogator paired with NanZee Technology's NZS-DSS-C07 optical fiber sensors. Specifically, the LUNA company utilizes distributed FOS (DFOS) technology that is capable of specifying spatial resolutions. The sensing fiber was precisely installed along the longitudinal axis of the carbon fiber central tube using a surface-adhered configuration. The DFOS sensor system specifications are comprehensively documented in Table 4. For independent validation of reconstructed displacements and rotations, a multi-camera Vicon Vero motion-capture system was deployed in the wind tunnel. Reflective markers mounted near the trailing edge of the flexible-wing prototype enabled optical measurement of wing deformation. The Vicon Vero motion-capture system's specifications are summarized in Table 5.

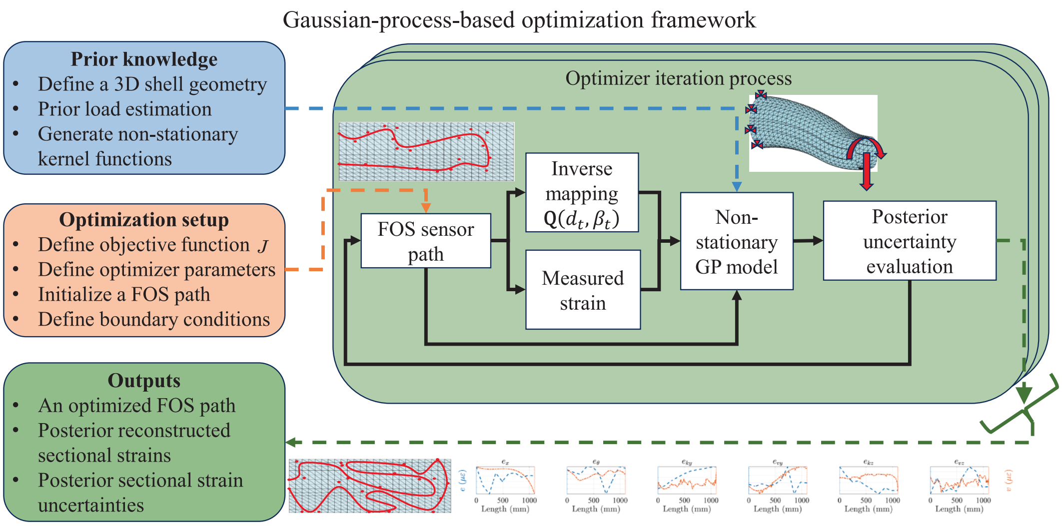

Fig. 4. Schematic diagram of the proposed Gaussian-process-based optimization framework.

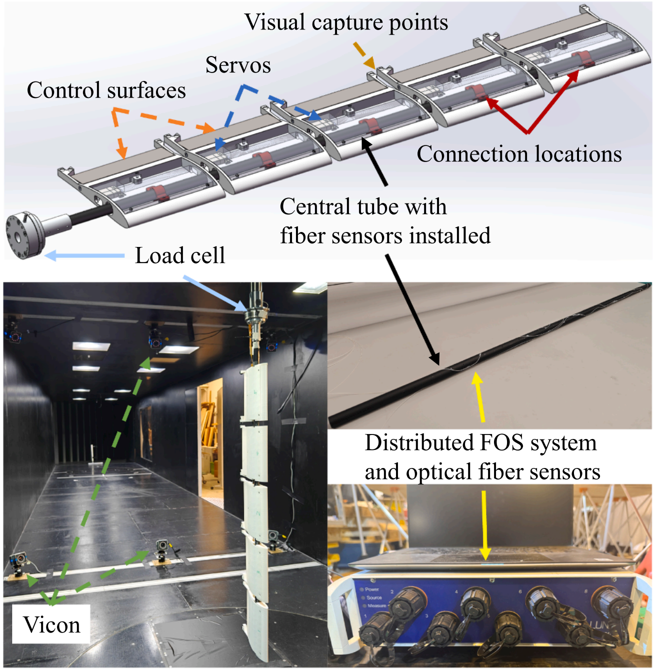

Fig. 5. Flexible wing prototype and hardware for simulation and wind tunnel experiment.

Table 1
Flexible wing prototype parameters.

Parameters	Values
Semi-span	1100 mm
Chord length	230 mm
Aspect ratio	9.57
Airfoil type	NACA 4415
Control surface chord length	46 mm
Central tube diameter	20 mm
Central tube thickness	0.5 mm
Flexibility	18% max deformation of the semi-span

Table 2
Digital servo parameters.

Parameters	Values
Operational speed	0.14 s/60° @ 6 V
Stall torque	5.5 kg·cm @6 V
Dimension	30 × 10 × 29.6 mm

4.2. *Simulation verification of Gaussian-process-based DFOS sensor placement*

In practical applications of flexible wings, it is commonly assumed that the wing operates under trimmed flight conditions. However, to induce significant deformation across all six DOFs, including axial extension, torsional deformation, bidirectional bending, and biaxial shear, all five control surfaces must be simultaneously deflected to their maximum limits. This configuration is selected because it typically generates the highest aerodynamic loading on the wing structure. The proposed GP-based optimization of DFOS sensor placement is expected to reduce uncertainty and improve reconstruction performance by at least 30% compared to conventional methods. Three DFOS sensor placements are compared to show the effectiveness of the proposed placements. They are.

- Straight path (SP) [14],
- Straight and sine path (SSP) [40],

Table 3
Load cell parameters.

Measurement	Range	Resolution
F_x, F_y	± 1900 N	0.32 N
F_z	± 3800 N	0.42 N
M_x, M_y, M_z	± 80 N • m	0.013 N • m

- Proposed GP-based optimized path (GPOP).

The path of the DFOS is presented in Fig. 6 and Fig. 7, where the length equals zero, indicates the wing root. These DFOS sensor placements rely on the same prior assumption regarding aerodynamic load distribution and utilize 200 uniformly distributed measurement points. The positions of SP and SSP are chosen to fall at ± 45° from the upper half of the cross-section of the circular tube, which allows for the simultaneous acquisition of strains in the y and z directions.

The prior understanding of the aerodynamic loads focuses on the flexible wing during the take-off phase, where the structure experiences maximum aerodynamic loading conditions. The resultant aerodynamic forces and moments are mathematically expressed as [41]

$$\begin{aligned}
\overline{q}_x(x) &= F_x(x), & \overline{M}_x &= \frac{1}{2}\rho V^2 c^2(x) C_{mx}(x),\\
\overline{q}_y(x) &= \frac{1}{2}\rho V^2 c(x) C_D(x), & \overline{M}_y &= \frac{1}{2}\rho V^2 S(x) C_{my}(x),\\
\overline{q}_z(x) &= \frac{1}{2}\rho V^2 c(x) C_L(x), & \overline{M}_z &= \frac{1}{2}\rho V^2 S(x) C_{mz}(x),
\end{aligned} \tag{41}$$

where $C_L(x)$, $C_D(x)$, $C_{mx}(x)$, $C_{my}(x)$, and $C_{mz}(x)$ are the dimensionless coefficients of lift, drag, torsional, in-plane, and out-of-plane bending coefficients, respectively. Within the bracket, variable x denotes the wing span coordinate. The distributed coefficient values are obtained from the OpenVSP analysis of the flexible wing prototype. $c(x)$ and $S(x)$ are the chord length and wing reference area with respect to the wing span, while ρ and V correspond to the air density and airflow velocity. $F_x(x)$ is the extensional force on the airfoil, which is assumed to be much smaller than lift and drag. To relate the sectional aerodynamic force and moment to the beam-element strain, the constitutive equations are defined as [21]

$$\begin{bmatrix} N \\ M_y \\ M_z \\ Q_z \\ Q_y \\ M_x \end{bmatrix} = \begin{bmatrix} A_x & & & & & \\ & D_y & & & & \\ & & D_z & & & \\ & & & G_z & & \\ & & & & G_y & \\ & & & & & J_x \end{bmatrix} \begin{bmatrix} e_1 \\ e_2 \\ e_3 \\ e_4 \\ e_5 \\ e_6 \end{bmatrix}, \tag{42}$$

where N, Q_y and Q_z are the forces along the x, y, and z directions, respectively. M_x, M_y and M_z are the moments along the x, y, and z directions, respectively. Term $A_x \equiv GA$ is the axial rigidity; $J_x \equiv GJ$ is the rotational rigidity; $G_y \equiv c_y^2 GA$ and $G_z \equiv c_z^2 GA$ are the shear rigidities, with c_y^2 and c_z^2 denoting the shear correction factors; $D_y \equiv EI_y$ and $D_z \equiv EI_z$ represent the bending rigidities.

Based on Eq. (42), each sectional strain component is directly associated with its corresponding sectional force or moment through the rigidity terms. It implies that the dominant load-transfer mechanism is uncoupled. Accordingly, the off-diagonal terms in the matrix-valued non-stationary covariance and in the associated Lipschitz measure are neglected in the practical implementation. The covariance kernel is therefore reduced from the matrix form to the diagonal form

$$\mathbf{k}(x, x') = \mathrm{diag}\left[k_j(x, x')\right], \ \ j = 1, \cdots, 6, \tag{43}$$

and the local derivative covariance becomes

Table 4
Distributed fiber optical sensing system specifications.

Parameters	Values
Fiber Diameter	0.9 ± 0.2 mm
Fiber type	SMG.652b
Strain measurement range	12,000 $\mu\varepsilon$
Resolution	1 $\mu\varepsilon$
Spatial resolution	1.3 mm, 2.6 mm, 5.2 mm
Measuring rate	50 Hz
Accuracy	± 25 $\mu\varepsilon$

Table 5
Vicon Vero motion-capture system specifications.

Parameters	Values
Resolution	2048 × 1088
Frame rate	100 Hz
Min standard FOV	44.1° × 23.6°
Min wide FOV	98.1° × 50.1°

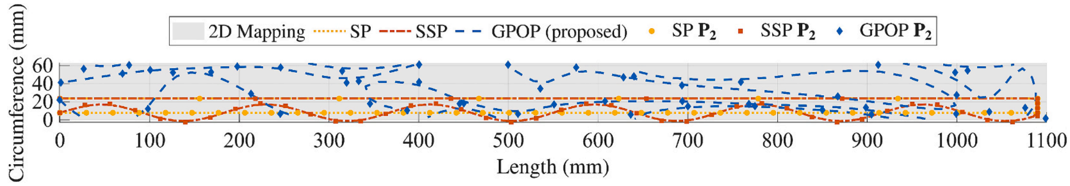

Fig. 6. The 2D path of the DFOS sensors, mounted along the carbon tube with periodic wrapping.

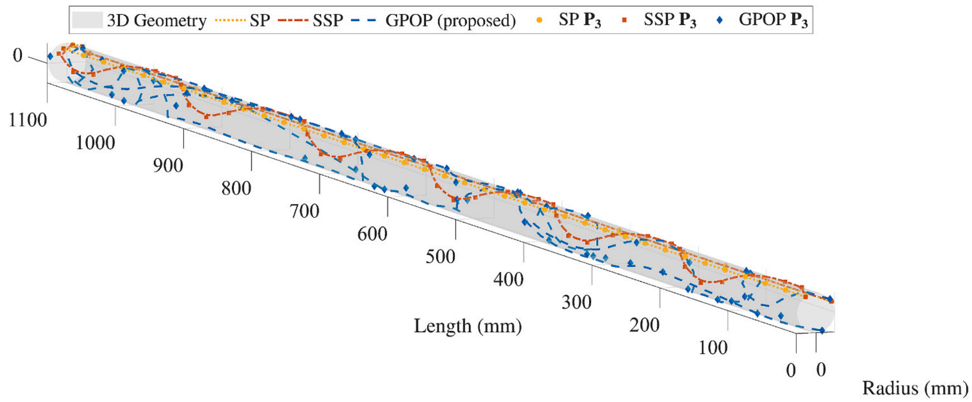

Fig. 7. The 3D path of the DFOS sensors, mounted along the carbon tube.

$$\mathrm{Var}(\mathbf{e}'(x)) = \mathrm{diag}\left[\frac{v_j^2(x)}{l_j^2(x)}\right], \quad j = 1, \cdots, 6, \tag{44}$$

where $v_j(x)$ and $l_j(x)$ denote the non-stationary uncertainty and length scale of the j-th sectional strain component, respectively. Consequently, Eqs. (23) and (25) are evaluated component-wise as

$$\widetilde{L}_j^{\max}(x) \propto \frac{v_j(x)}{l_j(x)}, \quad l_j(x) = \frac{v_j(x)}{\widetilde{L}_j^{\max}(x)}. \tag{45}$$

Thus, the prior understanding of aerodynamic loads on the non-stationary hyperparameters of the GP model would be connected through the equilibrium equation defined in Eq. (42) and the Lipschitz constant defined in Eq. (23) to (25). Fig. 8 presents the Lipschitz constant evaluated across five wing sections with respect to the spanwise coordinate, as well as the varying uncertainty magnitude and derived non-stationary length scale of the GP model. The Lipschitz-based smoothing regularization is introduced to constrain the variation of the non-stationary hyperparameters, so as to preserve the positive semi-definiteness of the covariance matrices and ensure robust probabilistic inference. At the same time, it retains the ability of the kernel to vary smoothly in space, which is necessary in the present aeroelastic application because non-uniform wing loading gives rise to localized variations in strain correlation and uncertainty.

Building upon the established prior understanding of the non-stationary hyperparameter, the posterior covariance distribution is derived for three paths. The spanwise representation of the posterior uncertainty evaluation is presented in Fig. 9 in percentage, which is obtained as $\overline{\mathbf{v}}_j^{\varepsilon}(x) = \mathbf{v}_j^{\varepsilon}(x)/v_j(x)$. The reconstructed displacement and rotation results via iFEM are in Fig. 10. The error for the displacement and rotation is introduced as

$$e_U = |U_r - U|, \quad e_\theta = |\theta_r - \theta|, \tag{46}$$

where U_r and θ_r denote the reference displacement and rotation from the Abaqus simulation, and U and θ represent reconstructed displacement and rotation, respectively. It is worth noting that in the present study, the conversion from strain to displacement is carried out through a least-squares reconstruction procedure [42]. And the quantified error evaluation is summarized in Table 6.

In Fig. 9(a), the simulation results indicate that the proposed GPOP significantly reduces uncertainty in axial strain. The primary reason is that the multi-directional GPOP path within each beam element further enhances strain-decoupling capability compared with SSP. Torsional strain in Fig. 9(b), a primary deformation mode of the aircraft wing, exhibits notable uncertainty reduction. Compared to the SP, the GPOP and SSP reduce uncertainty by 54% and 19%, respectively. GPOP demonstrates superior performance, particularly within the 100 to 400 mm span range. This is further supported by the reconstructed torsional strain, which shows the smallest discrepancy from the Abaqus reference results.

Bending represents the dominant deformation mode in aerostructures, as it directly correlates with the curvature and shear strain of structural components. In Fig. 9(c) and (e), the SP, SSP, and GPOP have 98.2%, 95.1%, and 93.8% uncertainty reduction on κ_y, and 25.4%, 24.3%, and 21.8% uncertainty reduction on κ_z, respectively. The results indicate that the SP yields the lowest uncertainty for both curvature components, which aligns with its frequent use in DFOS monitoring studies [43,44]. However, a sharp turning in the wing tip of the SP results in an ill-conditioned system matrix as defined in Eq. (15). Consequently, the reconstructed bending displacements U_y and U_z diverge near the end of the tube, as presented in Fig. 10(c) and (e). In contrast, the SSP maintains low uncertainty in curvature while its additional spatial variation in shear and torsional directions provides sufficient information to ensure a full-rank iFEM matrix, enabling accurate displacement reconstruction. The GPOP path, while exhibiting the second-lowest uncertainty in lift-induced curvature, achieves the most accurate overall bending deformation reconstruction. This superior performance can be attributed to its significantly improved accuracy in shear strain estimation, which plays a critical role in the iFEM-based displacement reconstruction process. Specifically, for the more dominant shear strain component κ_z under lift loading, GPOP and SSP achieve 71.2% and 45.8% reductions in uncertainty, respectively, compared to the SP, as demonstrated in Fig. 9(d). The enhanced observability of shear strain in GPOP contributes to better conditioning of the iFEM system matrix, thereby enabling more accurate reconstruction of bending displacements. Despite slightly higher uncertainty in drag-induced curvature, it maintains a maximum reconstruction error in U_y of less than 3 mm.

Curvature uncertainty directly impacts the accuracy of reconstructed rotational angles. In Fig. 10(d) and (f), among the three trajectories, SP exhibits the smallest discrepancy in reconstructed θ_z, consistent with its lowest overall curvature uncertainty in the y-axis. However, despite GPOP having slightly higher curvature uncertainty on y and z directions compared to SSP, its lower uncertainty in other key strain components, particularly shear, contributes to superior rotation reconstruction performance under the iFEM framework. Furthermore, in the posterior uncertainty evaluation of curvature along the z-axis, GPOP outperforms the other trajectories in the 800 to 1000 mm region. This localized improvement leads to a notable reduction in reconstruction error for the rotational angle θ_y, further demonstrating the effectiveness of the GPOP path in capturing complex deformation behavior.

The high accuracy of the reconstructed displacements and rotations on GPOP provides a validated bridge from strain to structural response for aeroelastic measurement. Leveraging the stiffness relationship in Eq. (42), the corresponding aerodynamic forces and moments are conveniently inferred, enabling accurate estimation of static aeroelasticity.

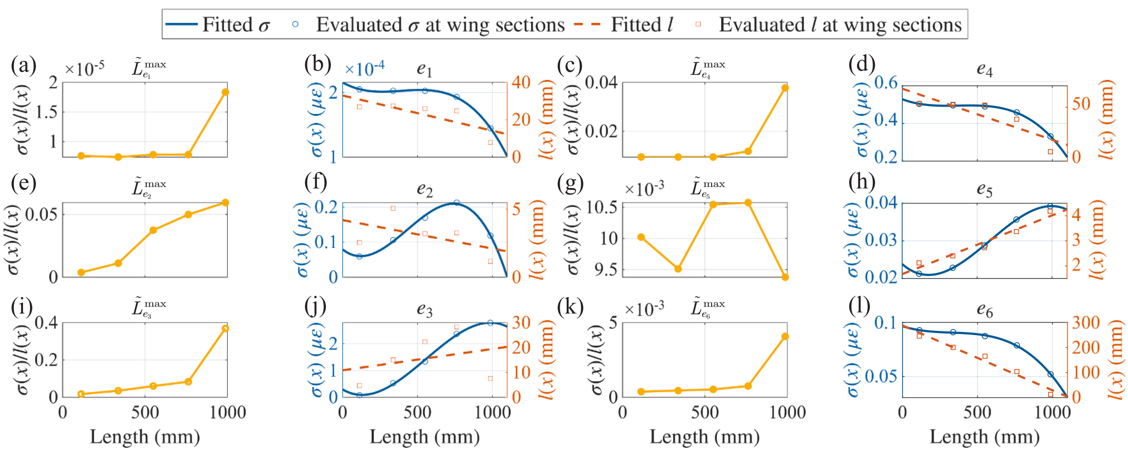

Fig. 8. Lipschitz constant and non-stationary hyperparameters evaluated at wing sections for 6 DOFs.

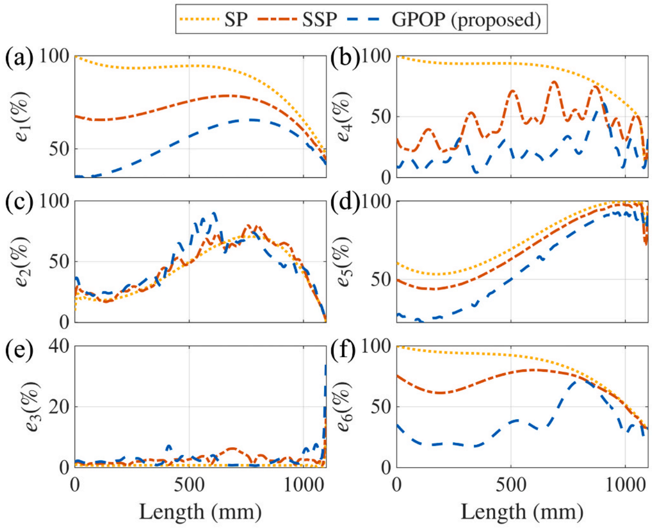

Fig. 9. Spanwise posterior uncertainty distribution of three DFOS sensor paths in percentage.

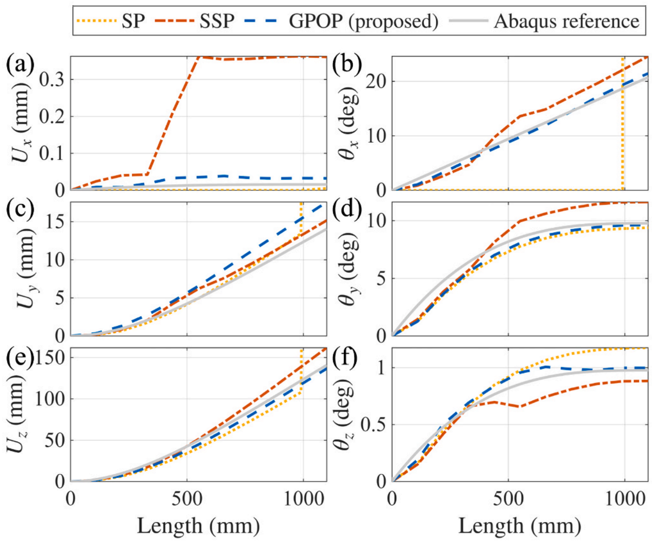

Fig. 10. Simulation comparison of reconstructed displacements and rotations.

Table 6
DFOS sensor's posterior uncertainty, displacement, and rotation comparison.

Path	$\|\mathbf{v}^{\epsilon}\|_2$ (με)	$\|\mathbf{v}^{\epsilon}\|_2$ (%)	$\|e_U\|_2$ (mm)	$\|e_\theta\|_2$ (deg)
GPOP	7.81	−52.72	20.62	4.01
SSP [40]	11.56	−30.02	35.16	13.18
SP [14]	16.52	0	6705.15	11738.10

4.3. Wind tunnel experiment verification of GP-based DFOS sensor placement optimization

The wind tunnel experiment was conducted with the same hardware configuration described in Section 4.1. The test conditions were a free-stream wind speed of 20 m/s and a body angle of attack of 2°. Two types of control surface excitations were applied, step and sinusoidal, which are demonstrated in Fig. 11. The step inputs consisted of deflections of 5°, 10°, and 15°, each held constant for 5 s, while the sinusoidal inputs had a frequency of 1.5 Hz and an amplitude of ± 8° over a duration of 7 s. Both excitation types were applied simultaneously to all five control surfaces. The step excitations are representative of maneuvers in flexible aircraft, particularly during takeoff, whereas the sinusoidal excitations were used to assess the accuracy of the dynamic response reconstruction. The spatial resolution of the DFOS was set to 5.4 mm. However, because different fiber paths correspond to different physical lengths, they contain different numbers of measurement points. To compare consistently, all path measurements are spatially interpolated into 400 uniformly distributed measurement points. The Vicon system employs six cameras to track a total of ten visual markers. The sampling frequencies are 50 Hz for the DFOS and 100 Hz for the Vicon system.

The Vicon records the space position of each visual capturing marker. It is necessary to reconstruct displacement and rotation in global coordinates. At each time frame t, the instant position is given by

$$\mathbf{P}_i^{(t)} = \mathbf{P}_i^{(0)} + \Delta\mathbf{P}_i^{(t)} = \mathbf{P}_i^{(0)} + \begin{bmatrix} \Delta x_i^{(t)} \\ \Delta y_i^{(t)} \\ \Delta z_i^{(t)} \end{bmatrix}, \tag{47}$$

where $\mathbf{P}_i^{(t)} \in \mathbb{R}^3$, and subscript i indicates the visual capturing marker. Therefore, it is convenient to obtain displacements as $\begin{bmatrix} U_x^{(t)} & U_y^{(t)} & U_z^{(t)} \end{bmatrix} = \begin{bmatrix} \Delta x^{(t)} & \Delta y^{(t)} & \Delta z^{(t)} \end{bmatrix}$. Rotational components are inferred from the spatial gradients of marker displacements along the wing span. The yaw angle θ_z and roll angle θ_y are approximated via linear regression of spanwise positions x against lateral and vertical displacements, respectively

$$\begin{aligned} \theta_y^{(t)}(x) &= \frac{\partial \Delta z}{\partial x}, \\ \theta_z^{(t)}(x) &= \frac{\partial \Delta y}{\partial x}. \end{aligned} \tag{48}$$

And torsional rotation $\theta_x^{(t)}$ is estimated by assuming that the markers lie on a circular arc whose radius is equal to the distance from the central tube to the marker. The pitch angle is computed from the tangential displacement in the $y-z$ plane

$$\theta_x^{(t)} = \arctan\left(\frac{\sqrt{(\Delta y)^2 + (\Delta z)^2}}{r}\right), \tag{49}$$

where term r represents the distance from the central tube to the marker that is located on the trailing edge of the flexible wing.

For displacement and rotation reconstructed from DFOS measurements, it should be noted that the SP configuration exhibits numerical divergence near the wing tip. Consequently, only the straight section of the SP is used for displacement and rotation reconstruction to ensure reliable results. In addition, small angular misalignments introduced during installation between the central tube and the airfoil connection points inevitably lead to data discrepancies between each path; thus, the wing tip reconstruction accuracy evaluation over the time span would be analyzed via normalized 2-norm error, which is defined as

$$\begin{aligned} e_U &= \sum\nolimits_{t=1}^{n} \left\| \frac{\left| U_r^{(t)}(L) - U^{(t)}(L) \right|}{U_r^{(t)}(L)} \right\|_2, \\ e_\theta &= \sum\nolimits_{t=1}^{n} \left\| \frac{\left| \theta_r^{(t)}(L) - \theta^{(t)}(L) \right|}{\theta_r^{(t)}(L)} \right\|_2, \end{aligned} \tag{50}$$

where U_r, θ_r, U, and θ denote the Vicon and DFOS displacement and rotation for three paths, respectively. The upperscript t denotes the

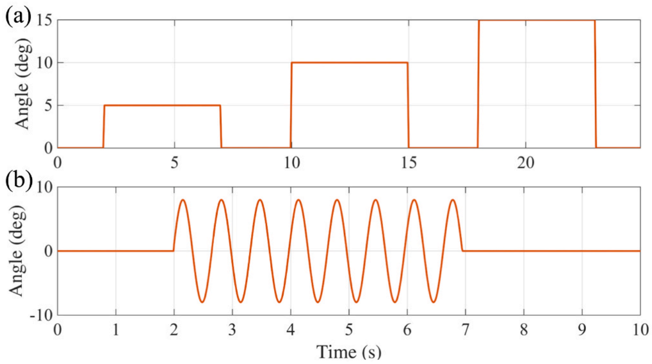

Fig. 11. Control surfaces excitation inputs for the wind tunnel experiment.

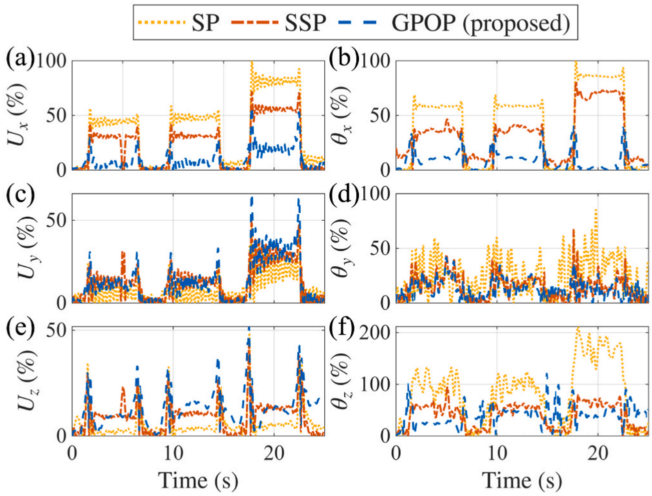

Fig. 12. Wind tunnel experiment comparison of the normalized error of wing tip displacements and rotations with control surfaces step excitation in percentage.

time frame, n denotes the number of time frames in total, and L represents the wing tip. It is worth noting that both the Vicon and DFOS reconstructed data are time-aligned and trimmed at the onset of the excitation to ensure a consistent comparison. The error of wing tip displacement and rotation comparison under step and sine excitation is represented in Fig. 12 and Fig. 13. And the quantified normalized error evaluation is summarized in Table 7.

In the step-excitation cases, the SP, SSP, and GPOP correctly reproduce the step-like deformation shape and its magnitude relative to the control surface inputs. The SP configuration exhibits the highest accuracy in reconstructing in-plane and out-of-plane wing-tip bending displacements, in agreement with the uncertainty assessment in Fig. 9. However, because only a single measurement orientation is available within each beam element, SP cannot decouple extensional and bending strain, and therefore cannot reconstruct extensional displacement as demonstrated in Fig. 12(a). In addition, as presented in the second column of Fig. 12, SP exhibits poor rotational reconstruction accuracy; in particular, θ_z response substantially overshoots the Vicon reference, yielding a 2-norm error of 209.6% and no reliable estimation of torsion. The SSP configuration, which employs a sinusoidal fiber path, introduces additional measurement angles and thereby improves reconstruction accuracy for extension, torsion, roll, and yaw by 33.7%, 27.3%, 8.9%, and 67.8%, respectively, at the cost of a slight degradation in in-plane and out-of-plane wing-tip bending displacement accuracy of 8.8% and 6.0%, relative to SP. The proposed GPOP configuration further enhances the overall performance, reducing extension, torsion, roll, and yaw errors by 70.2%, 78.3%, 16.0%, and 115.7%, respectively, compared with SP, while increasing in-plane and out-of-plane bending errors by only 13.6% and 11.7%. These results indicate that the GP-based optimization framework effectively predicts and mitigates reconstruction uncertainty.

In Fig. 13, the sinusoidal-excitation cases, the relative performance of SP, SSP, and GPOP follows the same qualitative trends as in

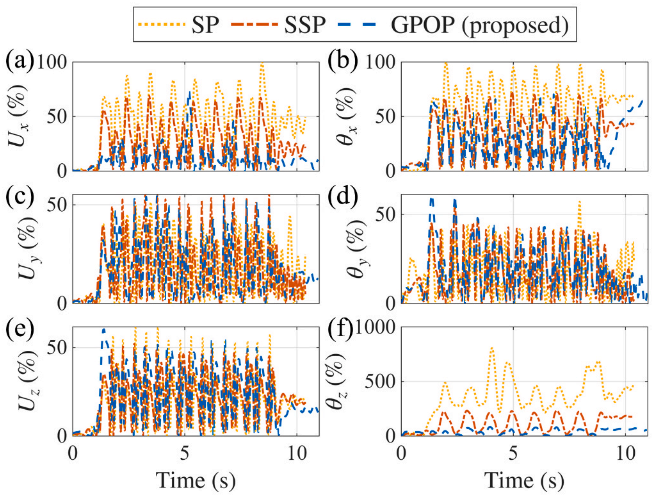

Fig. 13. Wind tunnel experiment comparison of the normalized error of wing tip displacements and rotations with control surfaces sinusoidal excitation in percentage.

Table 7
Normalized error assessment of tip displacement and rotational response, expressed as percentages, for all control surfaces under step and sinusoidal servo excitations.

DOFs	e_{U_x} (%)		e_{U_y} (%)		e_{U_z} (%)		e_{θ_x} (%)		e_{θ_y} (%)		e_{θ_z} (%)	
Servo	Step	Sine	Step	Sine	Step	Sine	Step	Sine	Step	Sine	Step	Sine
GPOP	29.8	47.6	42.2	45.1	27.2	42.7	21.7	51.1	34.8	46.7	93.9	87.3
SSP [40]	66.3	71.5	37.4	45.7	21.6	40.0	72.7	65.5	41.9	49.2	141.8	147.1
SP [14]	100	100	28.6	45.2	15.6	38.3	100	100	70.8	54.1	209.6	273.6

the step-excitation tests, but with reduced quantitative accuracy. This degradation arises mainly from two factors. Firstly, the lower sampling frequency of the DFOS system distorts the measured sinusoidal response, producing two apparent local peaks per cycle and thereby inflating the normalized error. Secondly, high-frequency vibration-induced noise introduces a phase mismatch between the Vicon and DFOS data, causing the error time histories to exhibit oscillations at an apparent frequency exceeding 1.5 Hz.

The reconstructed DFOS displacements and rotations spanning the wing root to the wing tip over 25 time instants are presented in Fig. 14 and Fig. 15, where the color bar indicates the error magnitude relative to the Vicon reference in percentage. The reconstruction performance over the time period is quantified by the average normalized spanwise reconstruction error, defined as

$$
\begin{aligned}
e_U &= \frac{1}{n}\sum_{t=1}^{n} \left\| \frac{\left|U_r^{(t)}(x) - U^{(t)}(x)\right|}{U_r^{(t)}(x)} \right\|_2, \\
e_\theta &= \frac{1}{n}\sum_{t=1}^{n} \left\| \frac{\left|\theta_r^{(t)}(x) - \theta^{(t)}(x)\right|}{\theta_r^{(t)}(x)} \right\|_2.
\end{aligned}
\tag{51}
$$

The numerically averaged normalized error evaluation over time is summarized in Table 8.

Focusing on the step-excited responses from Fig. 14(a1, a4, a7), the GPOP configuration shows that the reconstructed U_x distribution closely coincides with the Vicon reference over the entire span. In contrast, for SSP and SP, the reconstructed extensional displacement exhibits clear deviation from the Vicon curve at all plotted time instants. For U_y demonstrated in Fig. 14(a2, a5, a8), SSP and SP achieved higher wing tip reconstruction accuracy, but with a clear high-error region between 200 mm and 300 mm caused by discontinuities in the Vicon data. Even though the GPOP presents more errors at the wing tip for U_y reconstruction, the uncertainty analysis in Fig. 9 indicates that the GPOP uncertainty level around the 300 mm spanwise location is comparable to that of SP, where GPOP accurately reproduces the lateral displacement distribution in that region. From Fig. 14(a3, a6, a9), the straight trajectories in SP and SSP provide an advantage in capturing displacement in the lift direction, leading to superior wing-tip accuracy. Nonetheless, the curved path of the GPOP still maintains sufficient sampling of the out-of-plane deformation and reproduces the spanwise U_z field with only a 6.1% tradeoff relative to SP.

The comparison of reconstructed angles in Fig. 14(b) indicates that GPOP clearly outperforms SP and SSP on the θ_x response, both within the high-confidence reconstruction region between 200 mm and 500 mm and at the wing tip, in line with the GP optimization design objective of high torsional reconstruction accuracy. For θ_y and θ_z, the proposed GPOP outperforms SP and SSP not only in the wing tip accuracy but also over the span, indicating improved robustness and fidelity in the reconstruction of rotational degrees of freedom.

Under sinusoidal servo excitation, the DFOS data exhibit noticeably larger frame-to-frame fluctuations as presented in Fig. 15(a) and (b). Consistent with the step-excitation results, GPOP shows clear advantages in four DOFS; compared with SP, GPOP achieves reductions of 47.8% in extensional error, 68.7% in torsional error, 15.2% in roll angle error, and 49.0% in yaw angle error, at the expense of only modest increases of 10.0% and 11.5% in the in-plane and out-of-plane deformation errors, respectively. These trends are consistent with the uncertainty quantification results as presented in Fig. 9 and indicate that the proposed GPOP configuration can capture both static and dynamic aeroelastic responses with high accuracy.

In addition, full-time GIF animations of DFOS-reconstructed flexible wing prototype displacements and rotations, with the color bar indicating the sum of normalized error for 6 DOFs in percentage, as well as recorded wind tunnel experiments videos for the step and sinusoidal excitation cases, are provided as supplementary materials.

In summary, the wind tunnel experimental results demonstrate that the proposed GP-based optimization framework provides an effective and reliable means of designing DFOS paths for multi-DOF deformation reconstruction. In both step and sinusoidal excitation cases, the proposed GPOP consistently outperforms the baseline SP and SSP in the reconstruction of extension, torsion, roll, and yaw, while incurring only modest penalties in in-plane and out-of-plane bending accuracy. The observed trends agree well with the uncertainty quantification in Fig. 9, indicating that the GP-based framework can successfully predict and reduce reconstruction uncertainty through optimal sensor placement.

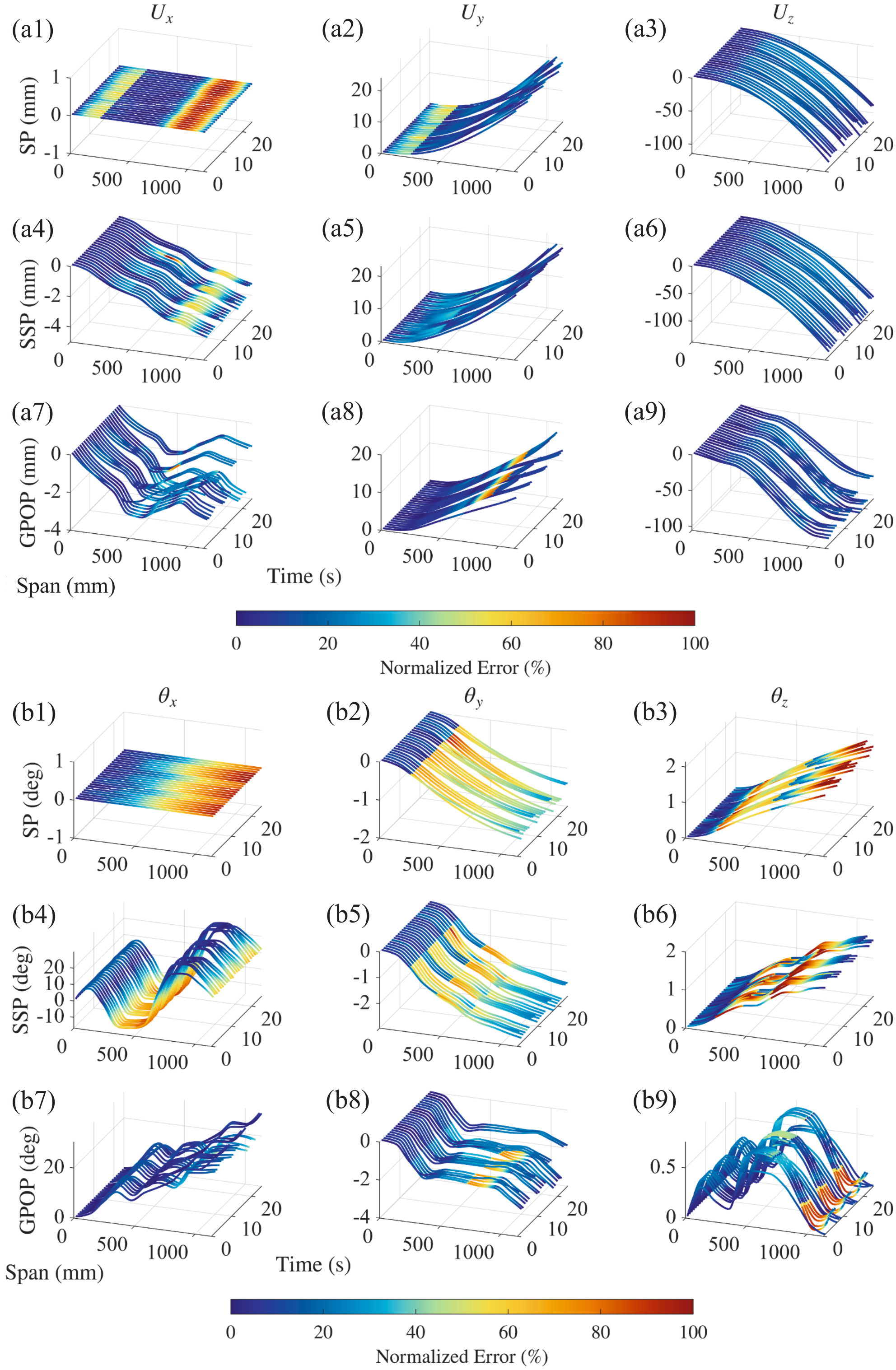

Fig. 14. Spanwise distribution of DFOS-reconstructed (a) displacement and (b) rotation under step excitation, with the color bar indicating the normalized deviation from the Vicon reference in percentage.

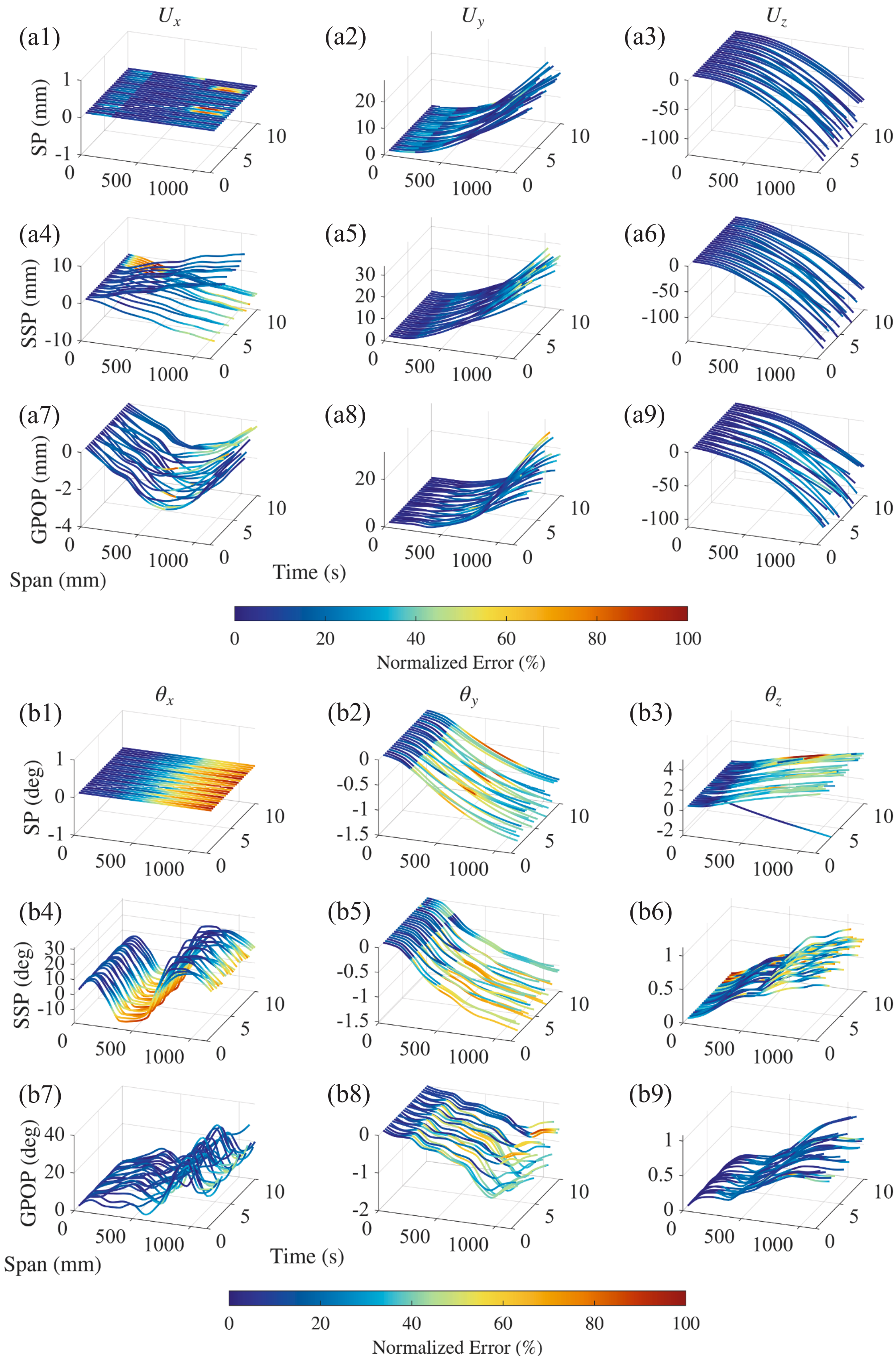

Fig. 15. Spanwise distribution of DFOS-reconstructed (a) displacement and (b) rotations under sinusoidal excitation, with the color bar indicating the normalized deviation from the Vicon reference in percentage.

Table 8
Time-averaged normalized error in spanwise displacement and rotational response, expressed as percentages, for all control surfaces under step and sinusoidal servo excitations.

DOFs	e_{U_x} (%)		e_{U_y} (%)		e_{U_z} (%)		e_{θ_x} (%)		e_{θ_y} (%)		e_{θ_z} (%)	
Servo	Step	Sine	Step	Sine	Step	Sine	Step	Sine	Step	Sine	Step	Sine
GPOP	56.6	52.2	42.9	41.2	26.7	26.8	13.3	31.3	51.2	59.4	80.7	50.6
SSP [40]	66.9	64.8	39.5	36.8	24.4	21.2	78.3	80.4	62.2	84.7	96.0	70.2
SP [14]	100	100	35.5	31.2	20.5	15.3	100	100	71.6	74.6	152.9	99.6

5. Conclusion

This paper presents a GP-based optimization framework for the design of FOS paths to improve displacement and rotation reconstruction of flexible wings. The wing is modeled using beam elements, whose sectional strains are represented as independent GP along the span, yielding closed-form posterior means and variances for each deformation degree of freedom. A nonstationary covariance, informed by Lipschitz-regularized aerodynamic loading, enables spatially adaptive correlations and rigorous uncertainty quantification over both instrumented and uninstrumented regions. Continuous FOS paths on shell surfaces are parameterized by combining conformal mapping and NURBS, which provides a distortion-aware planar domain and a low-dimensional set of path design variables. Sensor placement is then formulated as a posterior-uncertainty-minimization problem, leading to a GPOP for aeroelastic shape sensing. Comparative studies against conventional straight and sinusoidal FOS layouts, using both numerical simulations and wind tunnel experiments, demonstrate that GPOP substantially enhances the reconstruction of extension, torsion, roll, and yaw, while incurring only a modest loss in bending displacement accuracy. These results confirm the effectiveness of the proposed framework for information-optimal FOS placement in dynamic aeroelastic measurement and flexible structural health monitoring.

Declaration of generative AI and AI-assisted technologies in the manuscript preparation process

During the preparation of this work, authors used ChatGPT in order to revise the grammar. After using this tool/service, authors reviewed and edited the content as needed and take full responsibility for the content of the published article.

CRediT authorship contribution statement

Boge Dong: Writing – review & editing, Writing – original draft, Visualization, Validation, Software, Methodology, Formal analysis, Data curation, Conceptualization. **Yihan Mei:** Writing – review & editing, Validation, Software, Investigation, Data curation. **Xuanyi Lu:** Validation, Software, Investigation, Data curation. **Yi Zhou:** Validation, Software, Data curation. **Shenghan Zhang:** Writing – review & editing, Supervision, Project administration. **Wenjia Wang:** Writing – review & editing, Supervision, Methodology. **Molong Duan:** Writing – review & editing, Supervision, Resources, Project administration, Funding acquisition, Conceptualization.

Declaration of competing interest

The authors declare that they have no known competing financial interests or personal relationships that could have appeared to influence the work reported in this paper.

Acknowledgments

The authors acknowledge support from Prof. Wang, who provided valuable feedback on this work. The help from other researchers is sincerely appreciated. The authors acknowledge support from the Innovation and Technology Fund (GHP/170/22SZ), the Research Grants Council (RGC) of the Government of Hong Kong Special Administrative Region (HKSAR) with RGC/ECS Projects (No. 26215824 and No. 26209123), as well as the Commercial Aircraft Corporation of China with sponsored project COMAC26EG02.

Appendix A. Supplementary data

Supplementary data to this article can be found online at https://doi.org/10.1016/j.ymssp.2026.114426.

Data availability

Data will be made available on request.

References

[1] M. Duan, I.V. Kolmanovsky, C.E. Cesnik, "Maneuver load Alleviation of very Flexible Aircraft via Nonlinear Decoupling Control," AIAA Scitech 2021, Forum (2021), https://doi.org/10.2514/6.2021-0501.

[2] M. Duan, J.H. Hansen, I.V. Kolmanovsky, C.E.S. Cesnik, Maneuver Load Alleviation of Flexible Aircraft through Control Allocation: a Case Study using X-HALE. International Forum on Aeroelasticity and Structural Dynamics (IFASD 2019), 2019.

[3] S.S. Graves, A.W. Burner, J.W. Edwards, D.M. Schuster, Dynamic Deformation Measurements of an Aeroelastic Semispan Model, J. Aircr. 40 (5) (2003) 977–984, https://doi.org/10.2514/2.6883.

[4] H.V. de Figueiredo, D.F. Castillo-Zúñiga, N.C. Costa, O. Saotome, R.G.A. da Silva, Aeroelastic Vibration Measurement based on Laser and Computer Vision Technique, Exp. Tech. 45 (1) (2021) 95–107, https://doi.org/10.1007/s40799-020-00399-0.

[5] G. Ding, X. Yan, X. Gao, Y. Zhang, S. Jiang, Reconstruction of Propeller Deformation based on FBG Sensor Network, Ocean Eng. 249 (2022), https://doi.org/10.1016/j.oceaneng.2022.110884.

[6] S. Weber, T. Kissinger, E. Chehura, S. Staines, J. Barrington, K. Mullaney, L.Z. Fragonara, I. Petrunin, S. James, M. Lone, R. Tatam, Application of Fibre Optic Sensing Systems to measure Rotor Blade Structural Dynamics, Mech. Syst. Sig. Process. 158 (2021) 107758, https://doi.org/10.1016/j.ymssp.2021.107758.

[7] K. Hoffmann, An Introduction to stress Analysis and Transducer Design using Strain Gauges, HBM (2012).

[8] Lokos, W., Olney, C., Chen, T., Crawford, N., Stauf, R., and Reichenbach, E., "Strain-Gage Loads Calibration Testing of the Active Aeroelastic Wing F/A-18 Aircraft," 2002. https://doi.org/10.2514/6.2002-2926.

[9] A. Bighashdel, H. Zare, S.H. Pourtakdoust, A.A. Sheikhy, An Analytical Approach in Dynamic Calibration of Strain Gauge Balances for Aerodynamic Measurements, IEEE Sens. J. 18 (9) (2018) 3572–3579, https://doi.org/10.1109/JSEN.2018.2815762.

[10] K. Hoffmann, An Introduction to Measurements using Strain Gages, Hottinger Baldwin Messtechnik GmbH, Darmstadt, 1989.

[11] Colomina, I., and Molina, P., "Unmanned Aerial Systems for Photogrammetry and Remote Sensing: A Review," ISPRS Journal of Photogrammetry and Remote Sensing. Volume 92, 79–97. https://doi.org/10.1016/j.isprsjprs.2014.02.013.

[12] E.J. Warrant, S. Johnsen, Vision and the Light Environment, Curr. Biol. 23 (22) (2013) R990–R994, https://doi.org/10.1016/j.cub.2013.10.019.

[13] I. Kressel, B. Dorfman, Y. Botsev, A. Handelman, J. Balter, A.C.R. Pillai, M.H. Prasad, N. Gupta, A.M. Joseph, R. Sundaram, M. Tur, Flight Validation of an embedded Structural Health monitoring System for an Unmanned Aerial Vehicle, Smart Mater. Struct. 24 (7) (2015) 075022, https://doi.org/10.1088/0964-1726/24/7/075022.

[14] R. Lance, J.R.P. Allen, P. Anthony, C. Patrick, P. Harmory, F. Pena, "NASA Armstrong Flight Research Center (AFRC). Fiber Optic Sensing System (FOSS), Technology" (2014).

[15] H.C. Hyer, D.C. Sweeney, C.M. Petrie, Functional Fiber-Optic Sensors embedded in Stainless Steel Components using Ultrasonic Additive Manufacturing for distributed Temperature and Strain Measurements, Addit. Manuf. 52 (2022), https://doi.org/10.1016/j.addma.2022.102681.

[16] P. Zhu, X. Feng, Z. Liu, M. Huang, H. Xie, M.A. Soto, Reliable packaging of Optical Fiber Bragg Grating Sensors for Carbon Fiber Composite Wind Turbine Blades, Compos. Sci. Technol. 213 (2021), https://doi.org/10.1016/j.compscitech.2021.108933.

[17] X. Liu, B. Jin, Q. Bai, Y. Wang, D. Wang, Y. Wang, Distributed Fiber-Optic Sensors for Vibration Detection, Sensors 16 (8) (2016) 1164, https://doi.org/10.3390/s16081164.

[18] M. Gherlone, P. Cerracchio, M. Mattone, M. Di Sciuva, A. Tessler, Shape Sensing of 3D Frame Structures using an Inverse Finite Element Method, Int. J. Solids Struct. 49 (22) (2012) 3100–3112, https://doi.org/10.1016/j.ijsolstr.2012.06.009.

[19] Ko, W. L., Richards, L., and Fleischer, V. T., "Applications of KO Displacement Theory to the Deformed Shape Predictions of the Doubly-Tapered Ikhana Wing," 2009.

[20] G. Cazzulani, A. Silva, P. Pennacchi, Optimization of Continuous Sensor Placement for Modal Analysis: Application to an Optical Backscatter Reflectometry Strain Sensor, Mech. Syst. Sig. Process. 150 (2021), https://doi.org/10.1016/j.ymssp.2020.107242.

[21] Y. Zhao, J. Du, H. Bao, Q. Xu, Optimal Sensor Placement for Inverse Finite Element Reconstruction of Three-Dimensional Frame Deformation, International Journal of Aerospace Engineering 2018 (2018), https://doi.org/10.1155/2018/6121293.

[22] H. Xu, Q. Zhou, L. Yang, M. Liu, D. Gao, Z. Wu, M. Cao, Reconstruction of Full-Field complex Deformed Shapes of Thin-Walled Special-Section Beam Structures based on in Situ Strain Measurement, Adv. Struct. Eng. 23 (15) (2020) 3335–3350, https://doi.org/10.1177/1369433220937156.

[23] Fu, Z., Zhao, Y., Bao, H., and Zhao, F., "Dynamic Deformation Reconstruction of Variable Section WING with Fiber Bragg Grating Sensors," Sensors (Switzerland), Vol. 19, No. 15, 2019. https://doi.org/10.3390/s19153350.

[24] Vazquez, S. L., Tessler, A., Quach, C. C., Cooper, E. G., and Spangler, J. L., "Structural Health Monitoring Using High-Density Fiber Optic Strain Sensor and Inverse Finite Element Methods," 2005.

[25] D.C. Kammer, Sensor Placement for On-Orbit Modal Identification and Correlation of Large Space Structures, J. Guid. Control Dynam. 14 (2) (1991) 251–259, https://doi.org/10.2514/3.20635.

[26] G.C. Kahandawa, J. Epaarachchi, H. Wang, K.T. Lau, Use of FBG Sensors for SHM in Aerospace Structures, Photonic Sensors 2 (3) (2012) 203–214, https://doi.org/10.1007/s13320-012-0065-4.

[27] R.F. Guratzsch, S. Mahadevan, Structural Health monitoring Sensor Placement Optimization under uncertainty, AIAA J. 48 (7) (2010) 1281–1289, https://doi.org/10.2514/1.28435.

[28] R.B. Gramacy, Surrogates Gaussian Process Modeling, Design, and Optimization for the Applied Sciences, Chapman and Hall/CRC (2020), https://doi.org/10.1201/9780367815493.

[29] W.-K. Hong, T.D. Pham, Reverse designs of Doubly Reinforced Concrete Beams using Gaussian Process Regression Models Enhanced by Sequence Training/Designing Technique based on Feature selection Algorithms, Journal of Asian Architecture and Building Engineering 21 (6) (2022) 2345–2370, https://doi.org/10.1080/13467581.2021.1971999.

[30] H. Rong, A.P. Teixeira, C. Guedes Soares, Ship Trajectory uncertainty Prediction based on a Gaussian Process Model, Ocean Eng. 182 (2019) 499–511, https://doi.org/10.1016/j.oceaneng.2019.04.024.

[31] A. Jain, T. Nghiem, M. Morari, R. Mangharam, "learning and Control Using Gaussian Processes" (2018), https://doi.org/10.1109/ICCPS.2018.00022.

[32] J.N. Hendriks, C.M. Wensrich, A. Wills, V. Luzin, A.W.T. Gregg, Robust Inference of Two-Dimensional Strain Fields from Diffraction-based Measurements, Nucl. Instrum. Methods Phys. Res., Sect. B 444 (2019) 80–90, https://doi.org/10.1016/j.nimb.2018.11.019.

[33] D. Poloni, D. Oboe, C. Sbarufatti, M. Giglio, Towards a Stochastic Inverse Finite Element Method: a Gaussian Process Strain Extrapolation, Mech. Syst. Sig. Process. 189 (2023) 110056, https://doi.org/10.1016/j.ymssp.2022.110056.

[34] Gherlone, M., Cerracchio, P., Mattone, M., and Sciuva, M. Di, "Dynamic Shape Reconstruction of Three-Dimensional Frame Structures Using the Inverse Finite Element Method," 2011.

[35] G. Di Leo, C. Liguori, A. Paolillo, Covariance Propagation for the uncertainty Estimation in Stereo Vision, IEEE Trans. Instrum. Meas. 60 (5) (2011) 1664–1673, https://doi.org/10.1109/TIM.2011.2113070.

[36] Huo, W., Liu, C., Du, Z., Jiang, X., Liu, Z., and Guo, X., "Topology Optimization on Complex Surfaces Based on the Moving Morphable Component Method and Computational Conformal Mapping," Journal of Applied Mechanics, Vol. 89, No. 5, 2022. https://doi.org/10.1115/1.4053727.

[37] Y. Yang, Z. Xu, M. Duan, Evolving Stress-Guided Continuous Fiber Path Optimization for Multi-Axis Additive Manufacturing of Composite Shells, Addit. Manuf. 113 (2025) 105012, https://doi.org/10.1016/j.addma.2025.105012.

[38] J. Piquee, I. López Canalejo, C. Breitsamter, R. Wüchner, K.-U. Bletzinger, Aerodynamic Analysis of a Generic Wing Featuring an Elasto-Flexible Lifting Surface, Adv. Aerodyn. 1 (1) (2019) 20, https://doi.org/10.1186/s42774-019-0022-7.

[39] J.-W. Lee, J.-H. Han, H.-K. Shin, H.-J. Bang, Active load Control of Wind Turbine Blade Section with Trailing Edge Flap: Wind Tunnel Testing, J. Intell. Mater. Syst. Struct. 25 (18) (2014) 2246–2255, https://doi.org/10.1177/1045389X14544143.

[40] Raman, V., Drissi-Habti, M., Limje, P., and Khadour, A., "Finer SHM-Coverage of Inter-Plies and Bondings in Smart Composite by Dual Sinusoidal Placed Distributed Optical Fiber Sensors," Sensors (Switzerland), Vol. 19, No. 3, 2019. https://doi.org/10.3390/s19030742.
[41] J.D. Anderson, Jr.,, "fundamentals of Aerodynamics" (2011).
[42] Hassani, S., and Dackermann, U., "A Systematic Review of Optimization Algorithms for Structural Health Monitoring and Optimal Sensor Placement," Sensors. 6. Volume 23. https://doi.org/10.3390/s23063293.
[43] M. Nicolas, R. Sullivan, W. Richards, Large Scale applications using FBG Sensors: Determination of In-Flight Loads and Shape of a Composite Aircraft Wing, Aerospace 3 (3) (2016) 18, https://doi.org/10.3390/aerospace3030018.
[44] Murayama, H., Tachibana, K., Hirano, Y., Igawa, H., Kageyama, K., Uzawa, K., and Nakamura, T., "Distributed Strain and Load Monitoring of 6 m Composite Wing Structure by FBG Arrays and Long-Length FBGs," 2012. https://doi.org/10.1117/12.970292.